Tracking the Morphological Evolution of Neuronal Dendrites by First-Passage Analysis

Fabian H. Kreten,[1,2] Barbara A. Niemeyer,[3,2] Ludger Santen,[1,2] and Reza Shaebani[1,2,*]

[1] *Department of Theoretical Physics, Saarland University, 66123 Saarbrücken, Germany*
[2] *Center for Biophysics, Saarland University, 66123 Saarbrücken, Germany*
[3] *Department of Molecular Biophysics, Center for Integrative Physiology and Molecular Medicine, School of Medicine, Saarland University, 66421 Homburg, Germany*

A high degree of structural complexity arises in dynamic neuronal dendrites due to extensive branching patterns and diverse spine morphologies, which enable the nervous system to adjust function, construct complex input pathways and thereby enhance the computational power of the system. Owing to the determinant role of dendrite morphology in the functionality of the nervous system, recognition of pathological changes due to neurodegenerative disorders is of crucial importance. We show that the statistical analysis of a temporary signal generated by cargos that have diffusively passed through the complex dendritic structure yields vital information about dendrite morphology. As a feasible scenario, we propose engineering mRNA-carrying multilamellar liposomes to diffusively reach the soma and release mRNAs, which encodes a specific protein upon encountering ribosomes. The concentration of this protein over a large population of neurons can be externally measured, as a detectable temporary signal. By developing a stochastic coarse-grained approach for first-passage through dendrites, we connect the model parameters to the characteristics of the evolving signal and, on the other hand, map them to the key morphological properties affected by neurodegenerative diseases— including the density and size of spines, the extent of the tree, and the segmental increase of dendrite diameter towards soma. Thus, we establish a direct link between the dendrite morphology and the statistical characteristics of the detectable signal. Our approach provides a fast noninvasive measurement technique to indirectly extract vital information about the morphological evolution of dendrites in the course of neurodegenerative disease progression.

The elaborate branching morphology of neuronal dendrites in advanced nervous systems allows the neuron to interact simultaneously with several neighbors through their axon terminals, leading to a complex network of signaling pathways [1, 2]. The diverse functions of dendritic trees are reflected in the broad variation of their architecture in different neuronal types and regions. The complex behavior of higher animals has also been attributed to the presence of small membranous protrusions called dendritic spines [3–6]. Functional synapses, as the basic computational units of signal transmission, consist of the presynaptic release site and dendritic protrusions, harbouring the signal recognition and transmission units. Spines play a vital role in neural functions such as cognition, memory, and learning [7–11] and often serve as the recipients of excitatory and inhibitory inputs in the mammalian brain and undergo dynamic structural changes regulated by neuronal activity [12, 13]. The morphology of spines plays a crucial role as, for example, the shape and size of spine head and neck determine the number of postsynaptic receptors and the generated synaptic current [8] and control the electrical and biochemical isolation of the spine from the dendrite shaft [14, 15].

Aging and several neurodegenerative diseases— e.g. fragile X and Down's syndromes, Alzheimer's disease, schizophrenia, and autism spectrum disorders— significantly influence the function of the nervous system by altering the morphology of dendrites [16–20]. These alterations occur in the overall extent of dendritic trees, the population of branches, the thickness and curvature of dendrite shafts, and the density, morphology, and spatial distribution of spines [21–34]. On the other hand, reversal of morphological changes upon treatment has also been reported [35, 36]. Despite the crucial importance of monitoring the structural evolution of dendritic trees and spines to diagnose and predict neurodegenerative diseases and to monitor success of potential treatments, noninvasive imaging of neuronal dendrites is currently infeasible. It is even highly challenging to collect statistically adequate structural information from direct invasive imaging due to technical limitations: Although image analysis techniques for 3D reconstruction of dendrites have been improved in recent years [37, 38], a high resolution image can be achieved by electron microscopy which is a very laborious technique and practically inappropriate for spatially large-scale investigations. Nevertheless, there exist powerful noninvasive techniques which allow real-time tracking of brain activities, ranging from electro- and magneto-encephalography for electric and magnetic field detection [39, 40] to nuclear magnetic resonance spectroscopy, positron emission tomography, and magnetic resonance imaging (MRI) for measuring the concentration of (neuro-)chemicals [41–44].

* Corresponding author. Email: shaebani@lusi.uni-sb.de.

In the absence of a direct efficient method for unraveling the microscopic morphology of spines and dendrites, we alternatively develop a fast noninvasive technique— based on processing an externally detectable signal generated by a large population of neurons— to indirectly obtain essential structural information. A possible realization of such a signal can be the concentration of an expressed protein by many neurons in the brain region of interest, monitored e.g. by the MRI technique. We discuss how mRNA-carrying multilamellar liposomes can reach a desired region of brain tissue using brain-targeted drug delivery techniques, pass through the complex dendrite structures to reach the soma, and release their mRNAs which encodes a specific protein upon encountering ribosomes (alternatively, liposomes could carry siRNA molecules to silence RNA and decrease a specific protein concentration). By analyzing the first-passage times of such cargos passing through the dendrite structure, we develop a framework that bridges the diverse morphological characteristics of dendrites and the statistical properties of the detectable evolving signal. Our technique enables systematic monitoring of neurodegenerative disease or treatment progression for individual patients.

Coarse-Grained Dendrite Model

To model the structure of dendrites we adopt a mesoscopic perspective and consider a regularly branched tree with n generations of junctions and a linear extent nL, with L being the average node-to-node distance. Notably, as we discuss below, our results remain valid for realistic degrees of global fluctuations of the structural parameters across the tree or local structural irregularities [45, 46]. By coarse-graining the stochastic transport inside dendrite shafts and spines, we study the hopping of noninteracting particles on the nodes of the tree; see [45] and Fig. 1. From a reservoir which initially contains $\mathcal{N}$ particles, each particle enters the tree at a random node with depth index $i \in [1, n]$ (with the depth level $i{=}n$ for dead ends and $i{=}0$ for soma) at a random entering time with mean value t_e. The entering times are drawn from a geometric distribution since the goal is to monitor a region of brain rather than the transport of a single particle. Assuming a uniform arrival position across the tree structure, the entry probability grows exponentially with the node depth in a binary branched tree, corresponding to the entry level distribution $E_i = \frac{2^{i-1}}{2^n-1}$ $(i \geq 1)$. At each time step, the particle either randomly hops to the neighboring nodes or waits, with probabilities q and $1-q$, respectively. The waiting probability takes into account the contribution of stochastic trapping events inside spines as well as the diffusion time inside the dendrite channel. We assume that the residence probability inside these biochemical cages is depth-independent since the spine number density along the dendrite is known to rapidly saturate after a short distance from the soma [37, 47]. The hierarchical increase of dendrite shaft diameter towards the soma is considered by introducing a topological bias parameter p which induces a directional preference

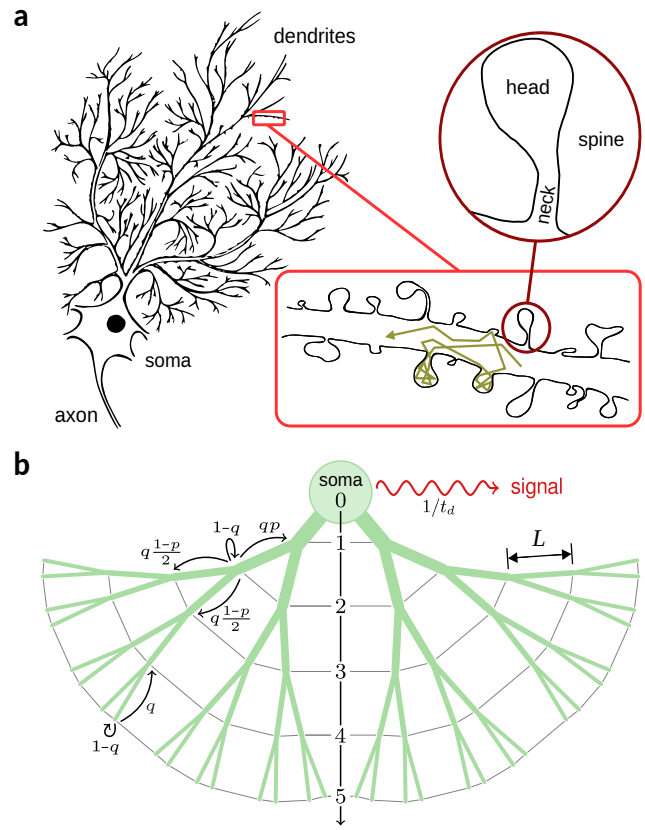

FIG. 1: Morphology of neuronal dendrites. (a) Schematic drawing of a neuron. Insets: (lower) A section of a typical dendritic channel. A sample path of a particle is shown; (upper) Structure of a mushroom-like spine. (b) Sketch of our binary tree model. A tree structure with depth $n = 5$ is depicted as an example. The possible choices at junctions or dead-ends are shown with arrows. The coarse-grained probability to reside inside spines is denoted with $1-q$, the topological bias p represents the segmental increase of dendrite diameter towards the soma, and $1/t_d$ denotes the pulse emission rate.

in the system: Jumping towards soma or dead ends occurs with probabilities p and $1-p$, respectively. The particle is eventually absorbed in the soma. After that, it takes a random time (called the emission time in the following) to emit a temporary pulse. The emission time is drawn from a geometric distribution with mean time t_d. We note that absorption in the soma and the considered type of signal emission are chosen as an example here but in general the boundary and initial conditions in our formalism can be adapted to any real experimental scenario.

We construct a set of coupled master equations for the time evolution of the probability $P_i(t)$ for a particle being at depth level i at time t, where the hopping and trapping probabilities on the network nodes are taken into

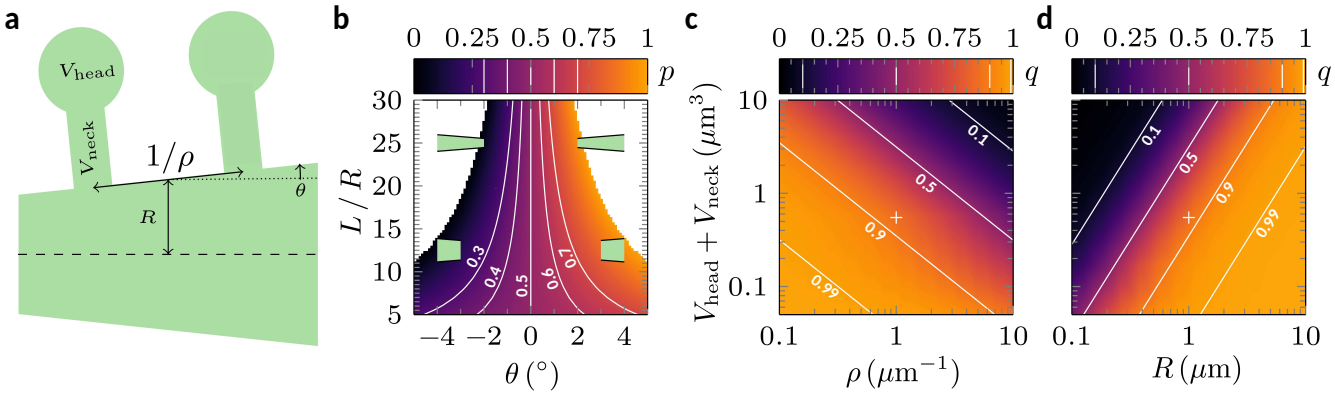

FIG. 2: Calibration of the mesoscopic model parameters. (a) Sketch of a section of the dendrite channel. (b) Bias probability p in terms of the opening angle θ and the ratio L/R between the mean branching distance L and mean channel radius R. The solid white lines represent isolines of constant p with the indicated values. The insets show schematic drawings of channel for different values of the (θ, L/R) set. (c),(d) Moving probability q in the ($V_{\rm head}$+$V_{\rm neck}$, ρ) and ($V_{\rm head}$+$V_{\rm neck}$, R) planes for the maximum possible time step $\Delta t = \frac{L^2}{2D}$. Other parameters: (c) $R = 1\mu$m, (d) $\rho = 1\mu{\rm m}^{-1}$. The solid white lines represent isolines of constant q with the indicated values. The crosses mark the set of parameter values ($V_{\rm head}$+$V_{\rm neck} = 0.55\,\mu{\rm m}^3$, $\rho = 1\,\mu{\rm m}^{-1}$, $R = 1\,\mu$m) for a typical healthy dendrite as a reference for comparison.

account; see *Suppl. Info.* for details. The resulting dynamics of individual particles can be described in general by stochastic two-state models [48, 49]. In particular, we previously derived the mean first-passage time (MFPT) of being absorbed in the soma (though for the initial condition of only entering from the dead ends) in terms of the structural parameters $\{n, q, p\}$ by treating the soma as an absorbing boundary [45, 46]. Importantly, we verified that the analytical predictions remain valid for realistic degrees of structural fluctuations (e.g., diversity in the extent of tree along different directions, disorder in the local branching patterns, etc.). Although the high sensitivity of the MFPT to the structural characteristics of dendrites is promising, MFPT is not a directly measurable quantity in dendrites. To realize the practical potential of our approach in technology and medicine, here we extend our proposed formalism and consider the subsequent steps after the particles reach the soma. We assume that each particle emits a temporary pulse after reaching the soma. The accumulation of the pulses generated in many neurons results in an evolving overall signal intensity $I(t)$ which can be detected externally. $I(t)$ contains the information of entering, first-passage, and emission times. It indeed reduces to the first-passage time distribution (though shifted by two time steps) in the limit of instantaneous entering and pulse emission, i.e. $t_e = t_d = 1$. For the general case of $t_e, t_d > 1$— where $I(t)$ deviates from the first-passage time distribution— we demonstrate how the statistical characteristics of $I(t)$ can be linked to the morphological properties $\{n, q, p\}$ of the dendrite structure.

Mapping to Real Dendrite Structures

We first verify the applicability of our mesoscopic approach by mapping the coarse-grained model parameters to the morphological characteristics of real dendrite structures. The depth parameter n and node-to-node distance L are directly mapped to the extent of the dendritic tree, which primarily depends on the nervous system and neuronal region and type. For instance, cerebellar Purkinje cells of guinea pigs extend up to $200\,\mu$m from the soma and have ~ 450 dendritic terminals [50]. This corresponds to nearly $n = 10$ generations of junctions which branch out around every $L = 20\,\mu$m.

To map the model parameters p and q to the structure of real dendrites, we consider the diffusive dynamics of a particle at a junction of the dendritic tree. The particle starts at a distance L from the neighboring junctions (see Suppl. Fig. S1). The bias parameter p results in unequal probabilities p and $1-p$ to reach the neighboring junction along the parent channel or child branches, respectively. To calibrate the probability of motion q, we equate the mean time to leave one node in the coarse-grained discrete time model with the mean travel time from the current junction to any of the neighboring ones in the presence of spines. We consider a symmetric branch at which the channels are connected with equal radii and without leaving a void space. The dynamics of the particle diffusing inside such a geometry can be effectively reduced to a one-dimensional diffusion in a single channel, described by the Fick-Jacobs equation

$$\frac{\partial}{\partial t}c(x,t) = D\frac{\partial^2}{\partial x^2}c(x,t) - D\frac{\partial}{\partial x}\Big(\frac{A'(x)}{A(x)}c(x,t)\Big) \qquad (1)$$

for the probability $c(x,t)$ of being at the projected posi-

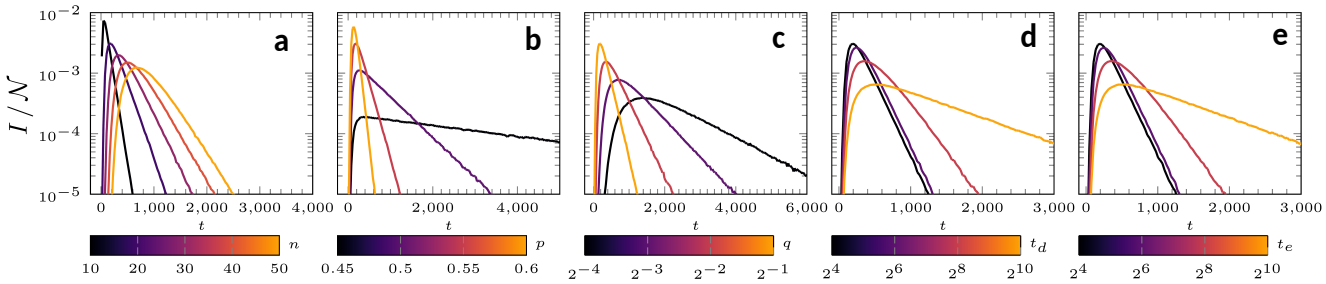

FIG. 3: Time evolution of the overall signal intensity I, scaled by the reservoir capacity $\mathcal{N}$ and averaged over bins of width 30 time steps, for different values of the model parameters. The reference parameter values are taken to be $n=20$, $p=0.55$, $q=0.5$, and $t_e=t_d=1$. The overall signal intensity is compared for different values of (a) n, (b) p, (c) q, (d) t_d, and (e) t_e. The selected values for each parameter are given in the color box of the respective panel.

tion x along the channel axis at time t [51]. $A(x)$ is the cross-sectional area of the channel and D is the diffusion constant inside it. The gradual thickening of the channel towards the soma is modeled by a conical channel shape given by $A(x)=\pi(R+\tan(\theta)(x-L))^2$, with R being the channel radius (at the junction) and θ the opening angle of the channel; see Fig. 2(a). The entrapment of particles inside spines leads to an effective diffusion constant $D_{\text{eff}}=D\,\frac{V_{\text{channel}}}{V_{\text{channel}}+V_{\text{spines}}}$, where V_{channel} is the volume of the channel segment and V_{spines} is the total volume of spines along it [52].

We analytically obtain the splitting probability and the mean escape time from the junction from Eq.(1) (see *Suppl. Info.* for details), leading to the following expressions for the bias and moving probabilities:

$$p=\frac{1}{2}\Big(1+\frac{L}{R}\tan(\theta)\Big), \tag{2}$$

$$q=\Delta t\frac{2D_{\text{eff}}}{L^2}=\Delta t\frac{2D}{L^2}\frac{1}{1+\dfrac{\rho(V_{\text{head}}+V_{\text{neck}})}{\pi R^2}}, \tag{3}$$

with Δt being the time resolution of measurements, V_{neck} and V_{head} the spine neck and head volumes, and ρ the spine density per length unit for regularly spaced spines along the channel; see Fig. 2(a). While no explicit bound is imposed on p and q by the above equations, both parameters are restricted due to the limited biologically relevant ranges of the structural parameters. For example, dendrite channels in cerebellar Purkinje cells lose less than $8\,\mu$m of their diameter along $200\,\mu$m length of the tree from soma to dendritic terminals [50], corresponding to an opening angle of less than 2° and $p\simeq 0.58$. We checked that $|\theta|\lesssim 5^\circ$ holds for several other examples of dendritic trees. Furthermore, $V_{\text{head}}+V_{\text{neck}}\simeq 0.5\,\mu\text{m}^3$ and $\rho\simeq 1\,\mu\text{m}^{-1}$ represent typical structural parameter values for a healthy dendrite [53]. We also note that the diffusion constant depends on the particle size. Some typical values are: $D\sim 20$ (green fluorescent protein (GFP) variants inside spines), ~ 100 (large Ca^{2+} ions inside spines), ~ 37 (photo activatable GFP, paGFP, inside dendrite channels), and $\sim 23.5\,\mu\text{m}^2/\text{s}$ (enhanced GFP, eGFP, inside the nucleus) [10, 54, 55]. Using these values, we obtain $t\simeq 0.8$, 0.5, and 0.2 s for the escape time of eGFP, paGFP, and Ca^{2+} from spines and $t\simeq 8.5$, 5.4, and 2.0 s for their travel time from one junction to the next one in a dendritic tree similar to that of cerebellar Purkinje cells but in the absence of spines.

The behavior of p and q versus the structural parameters of dendrites is shown in Figs. 2(b)-(d). It can be seen that both p and q vary monotonically with the structural parameters within their biologically relevant ranges, which allows for mapping of the morphological characteristics of real dendrite structures to the coarse-grained model parameters.

Signal Processing

To establish a direct link between the dendrite morphology and the statistical characteristics of the detectable signal, our next step is to demonstrate how the coarse-grained model parameters influence the time evolution of the overall signal. Figure 3 represents the typical time evolution of the signal intensity $I(t)$: It first develops a peak followed by an exponential decay at long times. However, the location and height of the peak and the slope of the tail depend on the model parameters. To clarify the influence of each parameter, we vary them separately in each panel of Fig. 3 and present the resulting signal intensities. By choosing $t_e=t_d=1$ in panels (a-c), the contribution of entering and emission times is turned off such that the signal intensity is equivalent to the first-passage time distribution of passing through the dendritic tree to reach the soma. While panels (a-c) focus on the role of the structural parameters $\{n,q,p\}$, panels (d,e) show how additional contributions of entering and emission time distributions lead to further broadening of $I(t)$. A common observation in all panels is the broadening of $I(t)$ and a slower decay of the tail accompanied by the reduction of the maximum intensity and a shift of the peak location to later times upon increasing the depth n of the tree (panel a), decreasing the bias p of motion

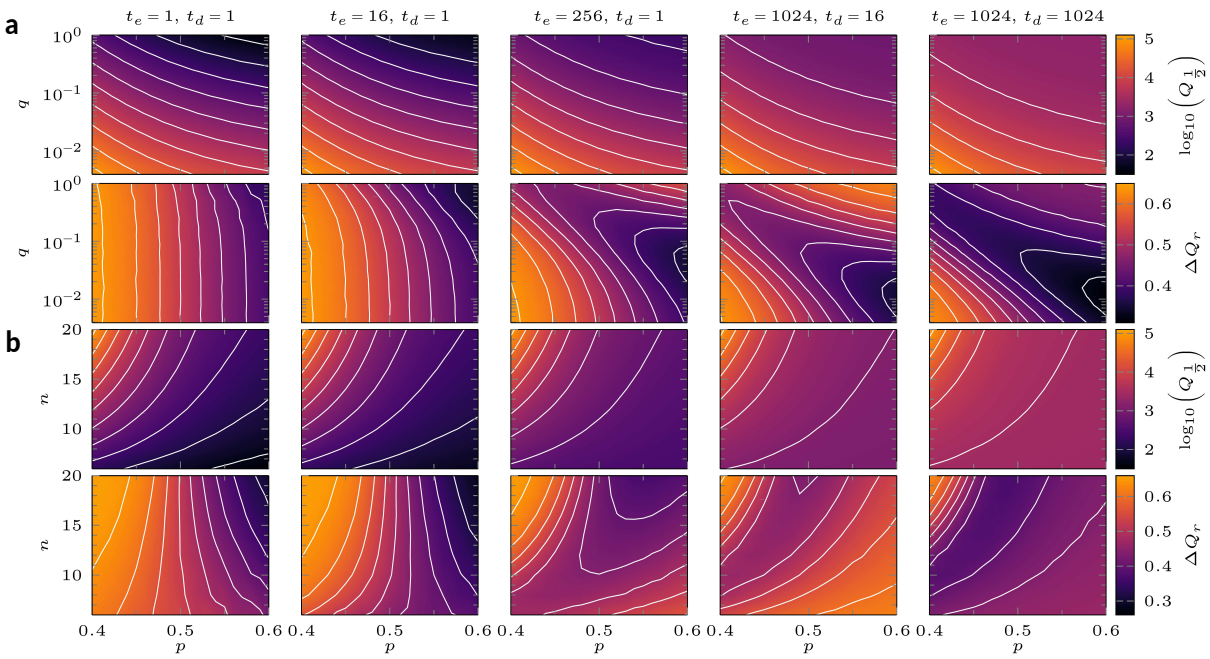

FIG. 4: Heat maps of the logarithm of the median, $\log_{10}(Q_{\frac{1}{2}})$, and the relative interquartile range, ΔQ_r, in (a) (q,p) and (b) (n,p) planes. Each column corresponds to a different set of mean entering and emission times. The same color coding is used for each row of heat maps. The isolines of constant $\log_{10}(Q_{\frac{1}{2}})$ or ΔQ_r are equidistantly chosen over the displayed range for each row. Other parameter values: (a) $n=10$, (b) $q=0.5$.

towards the soma (panel b), decreasing the probability q of being in the motion phase (panel c), or increasing the mean entering time t_e or emission time t_d (panels d and e). The change in the slope of the tail is particularly pronounced when passing the unbiased hopping threshold $p=0.5$ in panel b. Also note that the signal intensity is invariant under the swapping of t_e and t_d, and the asymptotic behavior is governed by the longest time scale. Overall, a faster arrival in the soma and/or a faster emission of the signal is associated with an earlier and higher peak and a steeper tail of $I(t)$.

To develop a more quantitative understanding of how key model parameters govern the signal intensity evolution, we vary n, q and p over the biologically relevant ranges and calculate various statistical characteristic of $I(t)$. For instance, the behavior of the logarithm of the median, $\log_{10}(Q_{\frac{1}{2}})$, is shown in Fig. 4 in the (q,p) or (n,p) planes for different choices of t_e and t_d (see also Suppl. Fig. S4 for other t_e and t_d values). The isolines of constant $\log_{10}(Q_{\frac{1}{2}})$ reveal that the median of the signal intensity varies monotonically in terms of the structural parameters. By increasing t_e and/or t_d, $\log_{10}(Q_{\frac{1}{2}})$ isolines shift to higher values but their shape remains unaffected. A similar behavior can be observed for the mean or maximum of $I(t)$. Thus, measuring the median of the signal intensity identifies isosurfaces in the (n,q,p) space (i.e. a set of admissible $\{n,q,p\}$ values), which is insufficient to uniquely determine these parameters. For a unique determination of the parameters $\{n,q,p\}$, additional statistical characteristics of $I(t)$ whose isolines behave differently from the median ones need to be extracted. We tested several quantities, amongst them the variance, skewness, etc. Their isolines behave differently from the median's ones but not significantly from each other. Additional independent quantities may be identified by analyzing other shape parameters of $I(t)$. Nevertheless, even two independent characteristics of $I(t)$ allow for identifying a one-dimensional manifold in the (n,q,p) space.

As the second quantity, we choose to work with the relative interquartile range ΔQ_r which is a measure of the statistical dispersion of $I(t)$ and has a smooth behavior upon varying the structural parameters. It is defined as $\Delta Q_r = \frac{Q_{3/4} - Q_{1/4}}{Q_{3/4} + Q_{1/4}}$, with $Q_{i/4}$ being the ith quartile (for example, the second quartile $Q_{2/4} \equiv Q_{1/2}$ corresponds to the median). The results shown in Fig. 4 reveal that the isolines of ΔQ_r and $\log_{10}(Q_{\frac{1}{2}})$ have distinctly different orientations at small t_e and t_d. In this regime, each pair of isolines for a measured set of $\log_{10}(Q_{\frac{1}{2}})$ and ΔQ_r intersect at a single point and the model parameter values can be determined uniquely. However, at longer t_e and t_d time scales, the isolines of ΔQ_r may exhibit a nonmonotonic behavior within the relevant range of the structural parameters or become nearly parallel to the isolines of $\log_{10}(Q_{\frac{1}{2}})$. As a result, each pair of isolines for

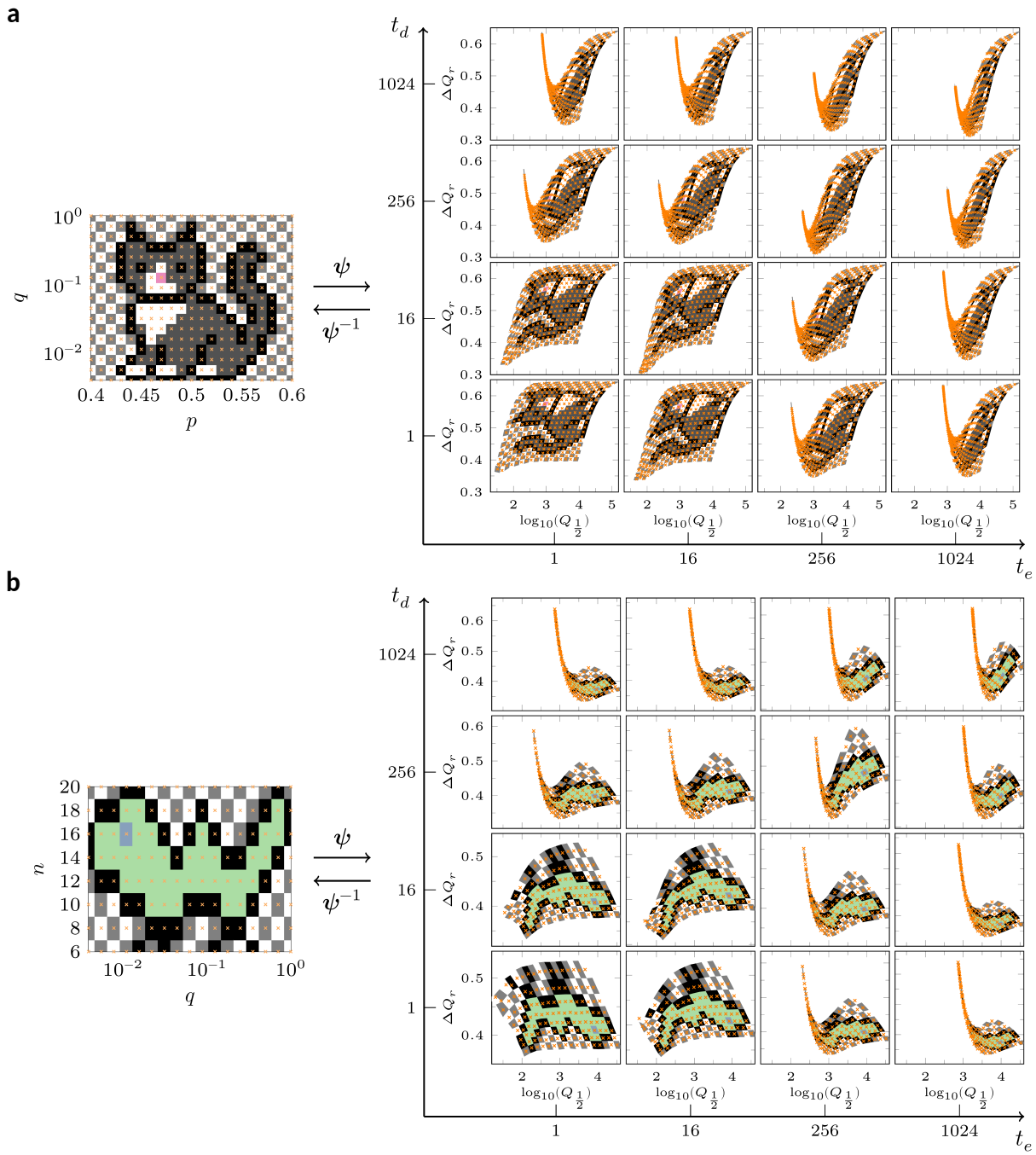

FIG. 5: Mapping the structural parameters to the characteristics of the signal intensity ($\boldsymbol{\psi}$), and vice versa ($\boldsymbol{\psi}^{-1}$). The mapping of (a) (p, q) and (b) (q, n) to $\left(\log_{10}(Q_{\frac{1}{2}}), \Delta Q_r\right)$ (i.e., the logarithm of the median and the relative interquartile range) is presented for different mean entering t_e and emission t_d times. Other parameter values: (a) $n = 10$, (b) $p = 0.55$. For every marked point on the structural parameter domain (yellow crosses), the corresponding location on the signal characteristic domain is extracted numerically. The neighborhood around each pair of connected points are painted with the same color in both domains for clarity.

a measured set of $\log_{10}(Q_{\frac{1}{2}})$ and ΔQ_r may have several intersections, meaning that $\{n, q, p\}$ parameters cannot be uniquely determined.

The sensitivity of the relation between the two sets of structural and signal intensity parameters to the choice of t_e and t_d time scales (shown in Fig. 4) can be more clearly presented in terms of the degree of information compression when mapping the phase spaces of these

two sets to each other. We denote the mapping of structure to signal and vice versa with $\boldsymbol{\psi}$ and $\boldsymbol{\psi}^{-1}$, respectively. Thus, the connection between the two sets can be represented as $\{\log_{10}(Q_{\frac{1}{2}}), \Delta Q_r\} = \boldsymbol{\psi}(n, q, p)$ and $\{n, q, p\} = \boldsymbol{\psi}^{-1}(\log_{10}(Q_{\frac{1}{2}}), \Delta Q_r)$ in general. In Fig. 5, we show the mapping of the (p, q) and (q, n) planes to the $\big(\log_{10}(Q_{\frac{1}{2}}), \Delta Q_r\big)$ plane for different mean entering t_e and emission t_d times; see also Suppl. Fig. S5 for the mapping of the (p, n) plane. We regularly sample the phase space of structural parameters (yellow crosses in left panels) and perform extensive simulations to obtain the signal intensity $I(t)$ and extract its median $\log_{10}(Q_{\frac{1}{2}})$ and dispersion ΔQ_r for each sampled set of $\{n, q, p\}$. For small values of t_e and t_d, the structure domain is mapped one-to-one to the signal domain. The mapping consists of a slightly skewed rotation and/or flip but mapping of two or more distinct points of the $\{n, q, p\}$ parameter space to a same point in the $\{\log_{10}(Q_{\frac{1}{2}}), \Delta Q_r\}$ space is unlikely, i.e., the map can be inverted. With increasing t_e and t_d, the high q regions in the structure domain gradually map to highly narrow regions in the signal domain. The compression of information to a space with one less dimension in the limit of large t_e and t_d time scales means that the map cannot be fully inverted anymore. To assess the invertibility limit of q, we quantify the compression of the points by the mapping from structure to signal domain; see *Suppl. Info.* for details. By setting a threshold level for the information compression, we can determine the maximum value of q (denoted by $q_{\max}$) up to which the map remains invertible (Suppl. Fig. S6). In Fig. 6(a), $q_{\max}$ is plotted as a function of $t_{\max} = \max(t_e, t_d)$, i.e., the longest time scale among the entering and emission times. It reveals that $q_{\max}$ decays with $t_{\max}$ roughly as a power-law, which can be presented as $q_{\max} \simeq \sqrt{\frac{\Delta t}{t_{\max}}}$ using the fact that $t_{\max}$ is measured in units of Δt. On the other hand, from Eq. [3] the maximum value of q for a given dendritic tree is obtained if spines are absent, leading to $q_{\text{spineless}} = \Delta t \frac{2D}{L^2}$ with D being the diffusion coefficient in the smooth channel without spines. The full range of q is invertible if $q_{\text{spineless}} \leq q_{\max}$, which imposes the constraint

$$\Delta t \leq \left(\frac{L^2}{2D}\right)^2 \frac{1}{t_{\max}} \tag{4}$$

on Δt, as plotted in Fig. 6(b) for different values of $t_{\max}$. For a given set of dendritic tree structure and tracer particle, the required time resolution of measurements Δt is inversely proportional to $t_{\max}$. The vertical lines in Fig. 6(b) mark the relevant range of $\frac{L^2}{D}$ for realistic values of the branching distance L and diffusion coefficients D for Ca^{2+}, fluorescein dextran (FD), and green fluorescent protein (GFP), as a few examples. It shows that a slower diffusion of tracer particles and shorter entering and emission times lead to a broader possible range for the time resolution of measurements Δt. For time resolutions around $\Delta t \simeq 0.04$ seconds (typical for currently available cameras) and tracer particles with diffusion coefficients similar to GFP, the required entering and emission times can be up to a few minutes. However, in special techniques such as nuclear magnetic resonance spectroscopy, one deals with time resolutions of several seconds, demanding more slowly diffusing particles and shorter entering and emission times on a sub-minute scale.

Morphological Changes during Disease Progression

The morphology of dendrites is broadly affected by aging [19, 21, 32] or neurodegenerative disorders such as Alzheimer's disease [19, 20, 22–24], autism spectrum disorders [19, 27–30], epilepsy disorder [59], schizophrenia [19, 25, 26], Down's syndrome [60], fragile X syndrome [30, 31], prion diseases [61], and stress-related disorders [62]. The affected morphological properties include the overall extent of dendritic tree, the segmental increase of dendrite diameter towards the soma, the population of branches, the thickness and curvature of dendrite shafts, and the morphology, density, and spatial distribution of spines. Here we clarify how these morphological changes influence our mesoscopic model parameters $\{n, q, p\}$. This information is then used in Fig. 6(c) to categorize the neurodegenerative disorders— those for which clear trends for the pathological changes of dendrite structure have been reported in the literature— based on the expected trends of the model parameters in the course of disease progression.

Variation of the extent of dendritic tree trivially influences the depth parameter n. Reduction of the tree extent is the observed trend during aging and several disorders such as Down's syndrome, schizophrenia, Alzheimer's disease, autism spectrum disorders, epilepsy disorder, stress-related disorders, Huntington's disease, etc. Increasing of the tree extent due to neurodegenerative disorders has not been reported to our knowledge.

The moving probability q, given by Eq. (3), is the only parameter affected by the presence of spines. q increases with decreasing spine size or density as observed, e.g., in aging, Down's syndrome, Alzheimer's disease, and schizophrenia; see Fig. 6(a) for an extended list of relevant disorders. Conversely, the spine density increases in a few cases such as autism spectrum disorders, fragile X syndrome, and hormonal imbalance, leading to the decrease of q. Nevertheless, the pathology of fragile X makes the prediction of q variations complicated: The increase of spine density (decrease of q) is accompanied by the shrinkage of spine size (increase of q); thus, the two effects compete and may even compensate each other such that q remains unchanged. The influence of hormonal imbalance on q depends on the hormone type and whether there is a deficiency or surplus.

The disorders that change the width of dendrite shafts influence the bias parameter p in general. Particularly, the decrease in dendritic arborization is often correlated with the overall reduction of the channel width. The details of width reduction determine the direction

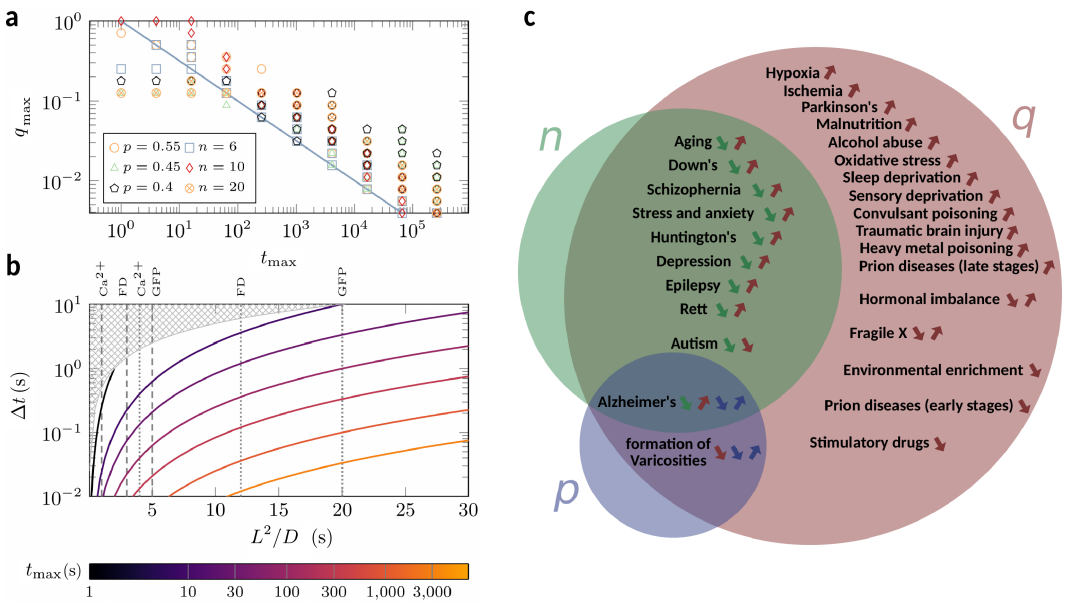

FIG. 6: (a) Invertibility threshold $q_{\max}$ versus the longest time scale $t_{\max}=\max(t_e, t_d)$ for different values of p and n. The line represents $q_{\max}=t_{\max}^{-1/2}$. (b) Time resolution of measurements Δt versus diffusive timescale L^2 / D for different values of $t_{\max}$. The hatched areas indicate the inadmissible region given by $\Delta t > L^2/2D$, where the probability q would be larger than one. The vertical lines mark the relevant range along the x-axis for Ca^{2+}, fluorescein dextran (FD), and green fluorescent protein (GFP) [54, 56]. (c) Pathologies of dendrite morphology, presented in terms of the mesoscopic model parameters n, p, and q (green, blue, and red colors, respectively). Each arrow indicates the increase or decrease of the corresponding parameter in the course of progression of the given disease. See [17, 57, 58] and references in the main text.

of changes of p: While a uniform reduction of channel radii effectively increases p (and decreases q), a radius-dependent reduction may change p in both directions. Moreover, an inhomogeneous spatial pattern of p can be caused by local changes of the channel width. For instance, local thinning of channel occurs in the vicinity of amyloid plaque deposition in Alzheimer's disease. Finally, the disorders that reduce the population of branches can increase the average node-to-node distance L, resulting in a larger p and smaller q and n.

We note that the pathology of spine and dendrite structure is more complicated in other diseases. For instance, distortion of spine shape observed in most mental retardations makes the prediction of the trend of q difficult. Despite the currently available information discussed above, there is a lack of quantitative studies to clarify the impact of various neurodegenerative disorders on dendritic spine, tree metric, and topological morphology.

Discussion

We have proven that the parameters $\{n, q, p\}$ of our mesoscopic model can be extracted by analyzing the detectable temporarily signal generated by a large population of neurons, provided that the time scales of entering the dendrites and emission of signal after reaching the soma are sufficiently small compared to the mean first-passage time of passing the dendritic tree. Although we constrained our analysis to signals formed by spontaneous pulses emitted by the particles in the soma with activation probability $\frac{1}{t_d}$, signals of other forms can be easily obtained from the signal studied in the present work. For example, if one seeks insight into the ability of neurons to integrate spine-derived (concentration) signals, the number of particles in the soma that have not yet emitted their pulse (i.e. are still active in this case) would be of interest. This quantity at time t is given by $t_d\, I(t{+}1)$, i.e. our measured signal shifted by one time step to the left and scaled by the mean activation time. In Suppl. Fig. S8, we present this signal alongside the time evolution of the fraction of particles in the soma that have not yet emitted their pulse for different values of t_e and t_d and for healthy versus differently degenerated dendritic trees.

On the other hand, the model parameters $\{n, q, p\}$ can be directly linked to the morphology of real dendrites via Eqs. (2) and (3). Since there are several morphological characteristics on the right hand sides of these equations, they cannot be uniquely determined by a given set of $\{n, q, p\}$. Nevertheless, most neurodegenerative disorders affect only a few of the morphological properties of dendrites. Therefore, by conducting regular patient monitoring for a given disease, the observed changes in

the parameters $\{n, q, p\}$ can be attributed to the changes of the morphological properties relevant to that specific disease. For instance, the growth rate of q and reduction rate of n for a patient with schizophrenia reflect, respectively, how fast the mean spine volume and the extent of dendritic tree are shrinking over time.

To link the detected signal intensity to the mesoscopic model parameters we have considered an ideal regular tree structure, while real dendritic trees are irregularly branched, spines have diverse sizes, and their spatial distribution is inhomogeneous. These fluctuations naturally cause variations in the corresponding model parameters $\{n, q, p\}$. However, we verified in our previous study [45] that the analytical results for the first-passage times of passing a regular tree structure remain valid when realistic degrees of global fluctuations of the structural parameters across the tree or local structural irregularities in the branching patterns are considered. Since the dependence of the signal intensity to the dendrite morphology is due to the contribution of the fist-passage times (and not the entering t_e and emission t_d times), we conclude that the presented results in the current study remain valid under typical structural irregularities and fluctuations observed in real neuronal dendrites.

We have characterized the behavior of the signal intensity $I(t)$ by two quantities, the logarithm of the median $\log_{10}(Q_{\frac{1}{2}})$ and the relative interquartile range ΔQ_r. The former is a representative of a category of the statistical measures including the mean, median, and maximum of $I(t)$. The latter quantifies the statistical dispersion of $I(t)$ and behaves similar to quantities such as the normalized variance and skewness. One may still identify further independent quantities by analyzing other moments of $I(t)$. Additional statistical measures of $I(t)$— which vary smoothly with the parameters $\{n, q, p\}$ and exhibit isolines that differ from those of $\log_{10}(Q_{\frac{1}{2}})$ and ΔQ_r— can in principle improve the accuracy of the extracted values of the model parameters $\{n, q, p\}$.

Our study focuses on solving the technical problem of processing the generated signal and linking it to the dendrite morphology. Nevertheless, preliminary steps should first be taken to generate the signal. This includes the transport of cargos to desired regions of brain tissue, entering the dendrites, travelling to the soma, and generating a temporary signal. Our proposed measurement procedure is summarized in Fig. 7(a). While addressing the technical issues of each preliminary step is beyond the scope of this study, obtaining a detectable signal is indeed feasible using the currently available technologies. In the following, we discuss possible methods for each of the measurement procedure steps:

1. **Transport of cargos to desired regions of brain tissue by means of brain-targeted drug delivery techniques.** Promising strategies have been developed so far to deliver drugs specifically to the brain to treat neurological disorders while minimizing systemic side effects [63–65]. Some of the currently feasible techniques include nanoparticle-based delivery [63, 66–73], focused ultrasound (non-invasive technique which offers spatially targeted drug delivery by transiently disrupting the blood-brain barrier (BBB) to pass through) [74], and carrier-mediated transport (utilizing endogenous transport systems like glucose or amino acid transporters facilitates drug transport across the BBB. Drug molecules are conjugated with ligands that target these transporters to enhance brain uptake) [75]. Moreover, injection into the spinal chord fluid or into ventricles could be an option to pass the BBB as well.

2. **Entering the neuronal dendrites and passing through their complex structure to reach the soma.** After reaching the area around the neurons, the contents of the cargos can enter the neuron by means of neuron-specific receptor-ligand binding [68–73]. This would mainly occur through the dendritic tree rather than axon or soma since the outer area of the neuron is mainly formed by the dendritic tree. Nevertheless, the contribution of entering from soma or axon to the generated signal can be evaluated and subtracted, as long as the axons and somata do not undergo morphological changes in the course of disease progression or treatment.

3. **Generating a temporary signal and detecting it.** Here, we mean any kind of detectable signal such as, but not limited to, electric or magnetic fields generated by many neurons. There are powerful noninvasive techniques for real-time tracking of brain activities. Electro- and magneto-encephalography for electric and magnetic field detection are established neurotherapeutic tools [39, 40]. Another possibility is to employ nuclear magnetic resonance spectroscopy (NMRS), which allows for noninvasive measurements of the concentration of different neuro-chemicals within a volume of brain down to a few cubic centimeters [41, 42]. The concentrations of substances generated in the somata of neurons can be obtained via NMRS with a time resolution of a few seconds which, depending on the diffusion constant of the particles, can remain within the feasibility range of our proposed method [76]. Positron emission tomography and magnetic resonance imaging (MRI) can be also employed to measure the concentration of neurochemicals [43, 44].

4. **Processing the evolving overall signal.** After detecting the signal, the approach developed in this paper enables one to process the signal intensity to uncover the morphology of dendrites.

As a more detailed plan for generating a detectable signal, we propose a protein expression scenario by injecting specific mRNAs carried by multilamellar liposomes;

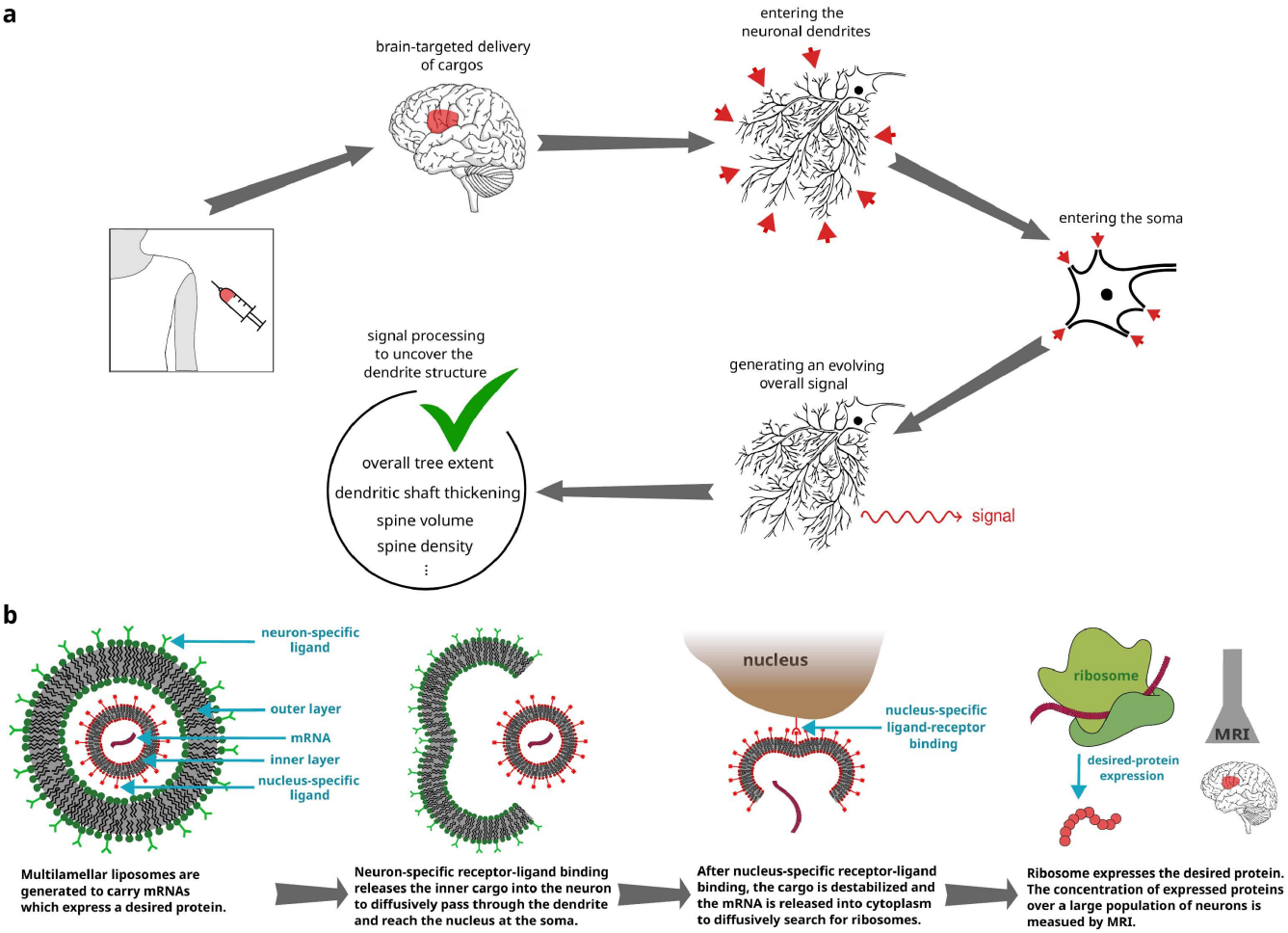

FIG. 7: (a) Schematic of our proposed noninvasive technique for a fast indirect measurement of the structural properties of dendrites based on processing a signal generated by a large population of neurons. By conducting regular measurements for a given patient, essential information about the morphological evolution of dendrites in the course of neurodegenerative disease or treatment progression can be extracted. (b) Schematic illustration of multilamellar liposomes designed to generate a specific protein. As a detectable temporary signal, the concentration of the expressed protein across the brain region of interest is externally monitored by the MRI technique.

see Fig. 7(b). The concept of producing multilamellar liposomes is currently feasible and has been realized in the context of cell activity regulation, immunotherapy, and vaccination [77–79]. Transport of liposomes to desired regions of brain and uptake of them by neurons have been feasible by modifying their surface with ligands targeting specific receptors on brain endothelial cells or neuronal dendrites [68–73]. Upon neuron-specific receptor-ligand binding, the multilamellar liposome enters the dendrite and loses its outer layer, leading to the release of the inner cargo into the cytoplasm. To enhance the dendrite specific entering, the endocytosis events around the synapses can be harnessed. For example, there is evidence that AMPA receptors are preferentially endocytosed around synapses [80]. The inner cargo is conjugated with nucleus-specific ligands [81–83] and diffuses inside the dendritic tree until it enters the soma and reaches the nucleus. The cargo can be designed to be destabilized or dissolved after the nucleus-specific receptor-ligand binding pins it to the exterior of the nucleus. This can be achieved, e.g., through specific proteolytic enzymes or pH-sensitive components in the cargo structure or adjusting the concentration of aqueous ionic solutions inside the cargo [84] to respond to the environmental differences between the region around the nucleus and the rest of the cytoplasm. The destabilized cargo releases mRNAs into the cytoplasm, which will diffusively search for ribosomes to produce a desired protein, such as ferritin. A typical neuron contains millions of ribosomes but their homeostatic distribution is still unknown [85, 86] (though recent studies revealed spacial inhomogeneities in the protein translation across the neuron, attributed to the spacial distribution of mRNAs and potential local specialization of ribosomes [86, 87]). The

expressed protein should be harmless and degrade over a reasonable time. Variations of the concentration of this protein over a large population of cells can be externally detected. For example, expression of ferritin can be monitored by the MRI technique [44]. We note that the presented formalism in the previous sections to obtain the first-passage time distribution of reaching the soma can be straightforwardly extended to calculate the additional first-passage time distribution of reaching from the soma to the distributed ribosomes. Moreover, here we considered a spontaneous signal emission but the formalism can be adapted to other scenarios such as a gradually degrading signal.

The clinical translation of these proposed techniques certainly requires rigorous testing and validation to ensure the safety and specificity of the novel approaches. Uptake and transport of cargos ca be initially tested, e.g., in cultured murine neurons. For the plan proposed in Fig. 7(b) based on the expression of proteins by ribosomes, spatial distribution of ribosomes in different types of healthy neurons needs to be determined. We expect that our proposals can potentially trigger active research and development in the fields of neuroscience, molecular engineering, and pharmacology.

To conclude, a framework has been developed to link the statistical characteristics of a detectable signal generated after reaching the somata of neurons to the morphological properties of neuronal dendrite structures. Our results open the possibility of indirectly monitoring the morphological evolution of dendrites in the course of neurodegenerative disorder progression. The mesoscopic approach presented in this study can be generalized to cope with further details of transport in real dendrite structures, such as handling the memory effects and aging inside spines [88] or to include active transport of cargos along microtubules [89]. Besides drawing conclusions regarding the morphological changes of dendrite structures, investigation of the first-passage properties of stochastic motion inside dendrites can deliver vital information about the ability to preserve local concentrations or induce concentration gradients of ions and molecules. These are tightly connected to neural functions and allow for drawing important physiological conclusions. The proposed approach also provides a route into a variety of other stochastic transport phenomena e.g. in varying energy landscapes, branched macromolecules and polymers, and labyrinthine environments with absorbing boundaries.

Materials and methods

The details of our mesoscopic model for cargo transport inside neuronal dendrites, calibration of the model parameters, clarification of the required time resolution of measurements, and estimation of the applicability range of our proposed technique are presented in the *Supporting Information* file.

Acknowledgments

We would like to thank Jochen Hub and Chetan Poojari for fruitful discussions and Anne Hafner for helping us with the schematic drawing of a neuron in Fig. 1. We acknowledge the use of GNU Parallel for scheduling and running our simulations in parallel [90]. This work was supported by the Deutsche Forschungsgemeinschaft (DFG) within the collaborative research center SFB 1027 and also via grants INST 256/539-1, which funded the computing resources at Saarland University. R.S. acknowledges support by the Young Investigator Grant of Saarland University, Grant No. 7410110401.

[1] Jan, Y.-N. & Jan, L. Y. Branching out: mechanisms of dendritic arborization. *Nat. Rev. Neurosci.* **11**, 316–328 (2010).

[2] Poirazi, P. & Papoutsi, A. Illuminating dendritic function with computational models. *Nat. Rev. Neurosci.* **21**, 303–321 (2020).

[3] Rasia-Filho, A. A., Calcagnotto, M. E. & von Bohlen und Halbach, O. *Dendritic Spines: Structure, Function, and Plasticity* (Springer International Publishing, Cham, Switzerland, 2023).

[4] Yuste, R. & Bonhoeffer, T. Genesis of dendritic spines: insights from ultrastructural and imaging studies. *Nat. Rev. Neurosci.* **5**, 24–34 (2004).

[5] Berry, K. P. & Nedivi, E. Spine dynamics: Are they all the same? *Neuron* **96**, 43–55 (2017).

[6] Hering, H. & Sheng, M. Dendritic spines: structure, dynamics and regulation. *Nat. Rev. Neurosci.* **2**, 880–888 (2001).

[7] Nicoll, R. A. A brief history of long-term potentiation. *Neuron* **93**, 281–290 (2017).

[8] Matsuzaki, M., Honkura, N., Ellis-Davies, G. C. R. & Kasai, H. Structural basis of long-term potentiation in single dendritic spines. *Nature* **429**, 761–766 (2004).

[9] Rogerson, T., Cai, D. J., Frank, A., Sano, Y., Shobe, J., Lopez-Aranda, M. F. & Silva, A. J. Synaptic tagging during memory allocation. *Nat. Rev. Neurosci.* **15**, 157–169 (2014).

[10] Bloodgood, B. L. & Sabatini, B. L. Neuronal activity regulates diffusion across the neck of dendritic spines. *Science* **310**, 866–869 (2005).

[11] Hongpaisan, J. & Alkon, D. L. A structural basis for enhancement of long-term associative memory in single dendritic spines regulated by pkc. *Proc. Natl. Acad. Sci. U.S.A.* **104**, 19571–19576 (2007).

[12] Bono, J., Wilmes, K. A. & Clopath, C. Modelling plasticity in dendrites: from single cells to networks. *Curr. Opin. Neurobiol.* **46**, 136–141 (2017).

[13] Moczulska, K. E., Tinter-Thiede, J., Peter, M., Ushakova, L., Wernle, T., Bathellier, B. & Rumpel, S. Dynamics of dendritic spines in the mouse auditory cortex during memory formation and memory recall. *Proc. Natl. Acad. Sci. U.S.A.* **110**, 18315–18320 (2013).

[14] Araya, R., Jiang, J., Eisenthal, K. B. & Yuste, R. The spine neck filters membrane potentials. *Proc. Natl. Acad. Sci. U.S.A.* **103**, 17961–17966 (2006).

[15] Noguchi, J., Matsuzaki, M., Ellis-Davies, G. C. R. & Ka-

sai, H. Spine-neck geometry determines NMDA receptor-dependent ca2+ signaling in dendrites. *Neuron* **46**, 609–622 (2005).

[16] Südhof, T. C. Neuroligins and neurexins link synaptic function to cognitive disease. *Nature* **455**, 903–911 (2008).

[17] Kulkarni, V. A. & Firestein, B. L. The dendritic tree and brain disorders. *Mol. Cell. Neurosci.* **50**, 10–20 (2012).

[18] Luebke, J. I., Weaver, C. M., Rocher, A. B., Rodriguez, A., Crimins, J. L., Dickstein, D. L., Wearne, S. L. & Hof, P. R. Dendritic vulnerability in neurodegenerative disease: insights from analyses of cortical pyramidal neurons in transgenic mouse models. *Brain. Struct. Funct.* **214**, 181–199 (2010).

[19] Penzes, P., Cahill, M. E., Jones, K. A., VanLeeuwen, J.-E. & Woolfrey, K. M. Dendritic spine pathology in neuropsychiatric disorders. *Nat. Neurosci.* **14**, 285–293 (2011).

[20] Dorostkar, M. M., Zou, C., Blazquez-Llorca, L. & Herms, J. Analyzing dendritic spine pathology in alzheimer's disease: problems and opportunities. *Acta Neuropathol.* **130**, 1–19 (2015).

[21] Petanjek, Z., Judas, M., Simic, G., Rasin, M. R., Uylings, H. B. M., Rakic, P. & Kostovic, I. Extraordinary neoteny of synaptic spines in the human prefrontal cortex. *Proc. Natl. Acad. Sci. U.S.A.* **108**, 13281–13286 (2011).

[22] Boros, B., Greathouse, K. M., Gentry, E. G., Curtis, K. A., Birchall, E. L., Gearing, M. & Herskowitz, J. H. Dendritic spines provide cognitive resilience against alzheimer's disease. *Ann. Neurol.* **82**, 602–614 (2017).

[23] Tackenberg, C., Ghori, A. & Brandt, R. Thin, stubby or mushroom: spine pathology in alzheimer's disease. *Curr. Alzheimer Res.* **6**, 261–268 (2009).

[24] Giannakopoulos, P., Gold, G., von Gunten, A., Hof, P. R. & Bouras, C. Pathological substrates of cognitive decline in alzheimer's disease. *Front. Neurol. Neurosci.* **24**, 20–29 (2009).

[25] Lewis, D. A. & González-Burgos, G. Neuroplasticity of neocortical circuits in schizophrenia. *Neuropsychopharmacol.* **33**, 141–165 (2008).

[26] Glausier, J. & Lewis, D. Dendritic spine pathology in schizophrenia. *Neurosci.* **251**, 90–107 (2013).

[27] Hutsler, J. J. & Zhang, H. Increased dendritic spine densities on cortical projection neurons in autism spectrum disorders. *Brain Res.* **1309**, 83–94 (2010).

[28] Toro, R., Konyukh, M., Delorme, R., Leblond, C., Chaste, P., Fauchereau, F., Coleman, M., Leboyer, M., Gillberg, C. & Bourgeron, T. Key role for gene dosage and synaptic homeostasis in autism spectrum disorders. *Trends Genet.* **26**, 363–372 (2010).

[29] Ford, T. J. L., Jeon, B. T., Lee, H. & Kim, W.-Y. Dendritic spine and synapse pathology in chromatin modifier-associated autism spectrum disorders and intellectual disability. *Front. Mol. Neurosci.* **15**, 1048713 (2023).

[30] Bagni, C. & Zukin, R. S. A synaptic perspective of fragile x syndrome and autism spectrum disorders. *Neuron* **101**, 1070–1088 (2019).

[31] Irwin, S. A., Patel, B., Idupulapati, M., Harris, J. B., Crisostomo, R. A., Larsen, B. P., Kooy, F., Willems, P. J., Cras, P., Kozlowski, P. B., Swain, R. A., Weiler, I. J. & Greenough, W. T. Abnormal dendritic spine characteristics in the temporal and visual cortices of patients with fragile-x syndrome: A quantitative examination. *Am. J. Med. Genet.* **98**, 161–167 (2001).

[32] Orner, D. A., Chen, C.-C., Orner, D. E. & Brumberg, J. C. Alterations of dendritic protrusions over the first postnatal year of a mouse: an analysis in layer vi of the barrel cortex. *Brain Struct. Funct.* **219**, 1709–1720 (2014).

[33] Tsai, J., Grutzendler, J., Duff, K. & Gan, W.-B. Fibrillar amyloid deposition leads to local synaptic abnormalities and breakage of neuronal branches. *Nat. Neurosci.* **7**, 1181–1183 (2004).

[34] Deng, Y.-P. & Reiner, A. Cholinergic interneurons in the q140 knockin mouse model of huntington's disease: Reductions in dendritic branching and thalamostriatal input. *J Comp. Neurol.* **524**, 3518–3529 (2016).

[35] Smith, D. L., Pozueta, J., Gong, B., Arancio, O. & Shelanski, M. Reversal of long-term dendritic spine alterations in alzheimer disease models. *Proc. Natl. Acad. Sci. U.S.A.* **106**, 16877–16882 (2009).

[36] Biscaro, B., Lindvall, O., Hock, C., Ekdahl, C. T. & Nitsch, R. M. Abeta immunotherapy protects morphology and survival of adult-born neurons in doubly transgenic app/ps1 mice. *J. Neurosci.* **29**, 14108–14119 (2009).

[37] Benavides-Piccione, R., Fernaud-Espinosa, I., Robles, V., Yuste, R. & DeFelipe, J. Age-based comparison of human dendritic spine structure using complete three-dimensional reconstructions. *Cereb. Cortex.* **23**, 1798–1810 (2013).

[38] Turner, N. L. *et al.* Reconstruction of neocortex: Organelles, compartments, cells, circuits, and activity. *Cell* **185**, 1082–1100 (2022).

[39] Nunez, P. L. & Srinivasan, R. *Electric Fields of the Brain: The neurophysics of EEG* (Oxford University Press, Oxford, UK, 2006).

[40] Hari, R. & Salmelin, R. Magnetoencephalography: From squids to neuroscience: Neuroimage 20th anniversary special edition. *NeuroImage* **61**, 386–396 (2012).

[41] Stanley, J. A. & Raz, N. Functional magnetic resonance spectroscopy: The new mrs for cognitive neuroscience and psychiatry research. *Front. Psychiatry* **9**, 76 (2018).

[42] Koolschijn, R. S., Clarke, W. T., Ip, I. B., Emir, U. E. & Barron, H. C. Event-related functional magnetic resonance spectroscopy. *NeuroImage* **276**, 120194 (2023).

[43] Bass, S. D., Mariazzi, S., Moskal, P. & Stepien, E. Colloquium: Positronium physics and biomedical applications. *Rev. Mod. Phys.* **95**, 021002 (2023).

[44] Liang, Z.-P. & Lauterbur, P. C. *Principles of Magnetic Resonance Imaging: A Signal Processing Perspective* (Wiley-IEEE Press, California, USA, 2000).

[45] Jose, R., Santen, L. & Shaebani, M. R. Trapping in and escape from branched structures of neuronal dendrites. *Biophys. J.* **115**, 2014–2025 (2018).

[46] Shaebani, M. R., Jose, R., Sand, C. & Santen, L. Unraveling the structure of treelike networks from first-passage times of lazy random walkers. *Phys. Rev. E* **98**, 042315 (2018).

[47] Ballesteros-Yanez, I., Benavides-Piccione, R., Elston, G. N., Yuste, R. & DeFelipe, J. Density and morphology of dendritic spines in mouse neocortex. *Neurosci.* **138**, 403–409 (2006).

[48] Shaebani, M. R. & Rieger, H. Transient anomalous diffusion in run-and-tumble dynamics. *Front. Phys.* **7**, 120 (2019).

[49] Shaebani, M. R., Rieger, H. & Sadjadi, Z. Kinematics of persistent random walkers with two distinct modes of

motion. *Phys. Rev. E* **106**, 034105 (2022).

[50] Rapp, M., Segev, I. & Yarom, Y. Physiology, morphology and detailed passive models of guinea-pig cerebellar purkinje cells. *J. Physiol.* **474**, 101–118 (1994).

[51] Jacobs, M. H. *Diffusion processes* (Springer, 1935).

[52] Dagdug, L., Berezhkovskii, A. M., Makhnovskii, Y. A. & Zitserman, V. Y. Transient diffusion in a tube with dead ends. *J. Chem. Phys.* **127**, 224712 (2007).

[53] Harris, K. M., Jensen, F. E. & Tsao, B. Three-dimensional structure of dendritic spines and synapses in rat hippocampus (ca1) at postnatal day 15 and adult ages: implications for the maturation of synaptic physiology and long-term potentiation. *J. Neurosci.* **12**, 2685–2705 (1992).

[54] Yasuda, R. & Murakoshi, H. The mechanisms underlying the spatial spreading of signaling activity. *Curr. Opin. Neurobiol.* **21**, 313–321 (2011).

[55] Chen, Y., Müller, J. D., Ruan, Q. & Gratton, E. Molecular brightness characterization of egfp in vivo by fluorescence fluctuation spectroscopy. *Biophys. J.* **82**, 133–144 (2002).

[56] Santamaria, F., Wils, S., De Schutter, E. & Augustine, G. J. Anomalous diffusion in purkinje cell dendrites caused by spines. *Neuron* **52**, 635–648 (2006).

[57] Fiala, J. C., Spacek, J. & Harris, K. M. Dendritic spine pathology: Cause or consequence of neurological disorders? *Brain Res. Rev.* **39**, 29–54 (2002).

[58] Maiti, P., Manna, J., Ilavazhagan, G., Rossignol, J. & Dunbar, G. L. Molecular regulation of dendritic spine dynamics and their potential impact on synaptic plasticity and neurological diseases. *Neurosci. Biobehav. Rev.* **59**, 208–237 (2015).

[59] Caznok Silveira, A. C., Antunes, A. S. L. M., Athie, M. C. P., da Silva, B. F., Ribeiro dos Santos, J. V., Canateli, C., Fontoura, M. A., Pinto, A., Pimentel-Silva, L. R., Avansini, S. H. & de Carvalho, M. Between neurons and networks: investigating mesoscale brain connectivity in neurological and psychiatric disorders. *Front. Neurosci.* **18**, 1340345 (2024).

[60] Marin-Padilla, M. Structural abnormalities of the cerebral cortex in human chromosomal aberrations: a golgi study. *Brain Res.* **44**, 625–629 (1972).

[61] Fuhrmann, M., Mitteregger, G., Kretzschmar, H. & Herms, J. Dendritic pathology in prion disease starts at the synaptic spine. *J. Neurosci.* **27**, 6224–6233 (2007).

[62] Christoffel, D. J., Golden, S. A. & Russo, S. J. Structural and synaptic plasticity in stress-related disorders. *Rev. Neurosci.* **22**, 535–549 (2011).

[63] Saraiva, C., Praca, C., Ferreira, R., Santos, T., Ferreira, L. & Bernardino, L. Nanoparticle-mediated brain drug delivery: Overcoming bloodâbrain barrier to treat neurodegenerative diseases. *J. Control. Release* **235**, 34–47 (2016).

[64] Juillerat-Jeanneret, L. The targeted delivery of cancer drugs across the bloodâbrain barrier: chemical modifications of drugs or drug-nanoparticles? *Drug Discov. Today* **13**, 1099–1106 (2008).

[65] Zhang, Z., Guan, J., Jiang, Z., Yang, Y., Liu, J., Hua, W., Mao, Y., Li, C., Lu, W., Qian, J. & Zhan, C. Brain-targeted drug delivery by manipulating protein corona functions. *Nat. Commun.* **10**, 3561 (2019).

[66] Yan, C., Gu, J., Yin, S., Wu, H., Lei, X., Geng, F., Zhang, N. & Wu, X. Design and preparation of naringenin loaded functional biomimetic nano-drug delivery system for Alzheimer's disease. *J. Drug Target.* **32**, 80–92 (2024).

[67] Nance, E. A., Woodworth, G. F., Sailor, K. A., Shih, T.-Y., Xu, Q., Swaminathan, G., Xiang, D., Eberhart, C. & Hanes, J. A dense poly(ethylene glycol) coating improves penetration of large polymeric nanoparticles within brain tissue. *Science Transl. Med.* **4**, 149ra119 (2012).

[68] Blasi, P., Giovagnoli, S., Schoubben, A., Ricci, M. & Rossi, C. Solid lipid nanoparticles for targeted brain drug delivery. *Adv. Drug Deliv. Rev.* **59**, 454–477 (2007).

[69] Gajbhiye, K., Pawar, A., Mahadik, K. & Gajbhiye, V. Pegylated nanocarriers: A promising tool for targeted delivery to the brain. *Colloids Surf. B Biointerfaces* **187**, 110770 (2020).

[70] Roney, C., Kulkarni, P., Arora, V., Antich, P., Bonte, F., Wu, A., Mallikarjuana, N., Manohar, S., Liang, H.-F., Kulkarni, A. R., Sung, H.-W., Sairam, M. & Aminabhavi, T. M. Targeted nanoparticles for drug delivery through the bloodâbrain barrier for alzheimer's disease. *J. Control. Release* **108**, 193–214 (2005).

[71] Schnyder, A. & Huwyler, J. Drug transport to brain with targeted liposomes. *NeuroRX* **2**, 99–107 (2005).

[72] Louiza Bohn Thomsen, M. S. T. & Moos, T. Targeted drug delivery to the brain using magnetic nanoparticles. *Ther. Deliv.* **6**, 1145–1155 (2015).

[73] Spuch, C. & Navarro, C. Liposomes for targeted delivery of active agents against neurodegenerative diseases (alzheimer's disease and parkinson's disease). *J. Drug Deliv.* **2011**, 469679 (2011).

[74] Hynynen, K., McDannold, N., Sheikov, N. A., Jolesz, F. A. & Vykhodtseva, N. Local and reversible bloodâbrain barrier disruption by noninvasive focused ultrasound at frequencies suitable for trans-skull sonications. *NeuroImage* **24**, 12–20 (2005).

[75] Pardridge, W. M. The blood-brain barrier: Bottleneck in brain drug development. *NeuroRX* **2**, 3–14 (2005).

[76] Gussew, A., Rzanny, R., Erdtel, M., Scholle, H. C., Kaiser, W. A., Mentzel, H. J. & Reichenbach, J. R. Time-resolved functional 1h mr spectroscopic detection of glutamate concentration changes in the brain during acute heat pain stimulation. *NeuroImage* **49**, 1895–1902 (2010).

[77] Tenchov, R., Bird, R., Curtze, A. E. & Zhou, Q. Lipid nanoparticles-from liposomes to mrna vaccine delivery, a landscape of research diversity and advancement. *ACS Nano* **15**, 16982–17015 (2021).

[78] Shi, C., Zhang, Q., Yao, Y., Zeng, F., Du, C., Nijiati, S., Wen, X., Zhang, X., Yang, H., Chen, H., Guo, Z., Zhang, X., Gao, J., Guo, W., Chen, X. & Zhou, Z. Targeting the activity of t cells by membrane surface redox regulation for cancer theranostics. *Nat. Nanotechnol.* **18**, 86–97 (2023).

[79] Moon, J. J., Suh, H., Bershteyn, A., Stephan, M. T., Liu, H., Huang, B., Sohail, M., Luo, S., Ho Um, S., Khant, H., Goodwin, J. T., Ramos, J., Chiu, W. & Irvine, D. J. Interbilayer-crosslinked multilamellar vesicles as synthetic vaccines for potent humoral and cellular immune responses. *Nat. Mater.* **10**, 243–251 (2011).

[80] Rosendale, M., Jullie, D., Choquet, D. & Perrais, D. Spatial and temporal regulation of receptor endocytosis in neuronal dendrites revealed by imaging of single vesicle formation. *Cell Rep.* **18**, 1840–1847 (2017).

[81] Jang, Y., Kim, W., Leblanc, P., Kim, C.-H. & Kim, K.-S. Potent synthetic and endogenous ligands for the adopted

orphan nuclear receptor nurr1. *Exp. Mol. Med.* **53**, 19–29 (2021).

[82] Sharma, S., Shen, T., Chitranshi, N., Gupta, V., Basavarajappa, D., Sarkar, S., Mirzaei, M., You, Y., Krezel, W., Graham, S. L. & Gupta, V. Retinoid x receptor: Cellular and biochemical roles of nuclear receptor with a focus on neuropathological involvement. *Mol. Neurobiol.* **59**, 2027–2050 (2022).

[83] DSouza, A., Nozohouri, S., Bleier, B. S. & Amiji, M. M. Cns delivery of nucleic acid therapeutics: Beyond the blood–brain barrier and towards specific cellular targeting. *Pharm. Res.* **40**, 77–105 (2023).

[84] Chu, B., Biriukov, D., Bischoff, M., PĹedota, M., Roke, S. & Marchioro, A. Evolution of the electrical double layer with electrolyte concentration probed by second harmonic scattering. *Faraday Discuss.* **246**, 407–425 (2023).

[85] Dastidar, S. G. & Nair, D. A ribosomal perspective on neuronal local protein synthesis. *Front. Mol. Neurosci.* **15**, 823135 (2022).

[86] Fusco, C. M., Desch, K., Dorrbaum, A. R., Wang, M., Staab, A., Chan, I. C. W., Vail, E., Villeri, V., Langer, J. D. & Schuman, E. M. Neuronal ribosomes exhibit dynamic and context-dependent exchange of ribosomal proteins. *Nat. Commun.* **12**, 6127 (2021).

[87] Glock, C., Biever, A., Tushev, G., Nassim-Assir, B., Kao, A., Bartnik, I., tom Dieck, S. & Schuman, E. M. The translatome of neuronal cell bodies, dendrites, and axons. *Proc. Natl. Acad. Sci. U.S.A.* **118**, e2113929118 (2021).

[88] Sadjadi, Z. & Shaebani, M. R. Orientational memory of active particles in multistate non-markovian processes. *Phys. Rev. E* **104**, 054613 (2021).

[89] Hafner, A. E., Santen, L., Rieger, H. & Shaebani, M. R. Run-and-pause dynamics of cytoskeletal motor proteins. *Sci. Rep.* **6**, 37162 (2016).

[90] Tange, O. *GNU Parallel 2018* (Ole Tange, 2018).